

metrical exciting line shapes may be treated by applying perturbation-theory methods to the approx-

imate solution of Eq. (21) beyond the level $U'' \approx 1$. This topic will be discussed more fully elsewhere.

*Work supported by the Petroleum Research Fund of The American Chemical Society.

¹L. I. Schiff, *Quantum Mechanics*, 3rd ed. (McGraw-Hill, San Francisco, 1968), p. 279.

²I. I. Rabi, *Phys. Rev.* **51**, 652 (1937).

³A. Abragam, *The Principles of Nuclear Magnetism* (Oxford U.P., London, 1961), p. 36.

⁴W. R. Salzman, *Phys. Rev. A* **4**, 1330 (1971).

⁵H. R. Reiss, *Phys. Rev. Letters* **25**, 1149 (1970).

⁶A. Ashkin, *Phys. Rev. Letters* **25**, 1321 (1970).

⁷The presentation of this section is essentially a re-

casting in general TLS notation of the presentation in K. Gottfried, *Quantum Mechanics* (W. A. Benjamin, New York, 1966), Vol. I, p. 427 ff.

⁸See, for example, S. S. Schweber, *An Introduction to Relativistic Quantum Field Theory* (Harper and Row, New York, 1961), p. 334.

⁹M. Born and E. Wolf, *Principles of Optics*, 3rd ed. (Pergamon, New York, 1965), p. 496.

¹⁰A. Yariv, *Quantum Electronics* (John Wiley, New York, 1967), p. 213.

¹¹For example, Ref. 1, p. 401 and Ref. 3, p. 28.

Computer Simulation of Electrical Breakdown in Gases; Avalanche and Streamer Formation*

Laurence E. Kline* and John G. Siambis

Department of Electrical Engineering, Carnegie-Mellon University, Pittsburgh, Pennsylvania 15213

(Received 6 July 1971)

This paper presents a new method for the simulation of electrical-breakdown phenomena, and plasma phenomena where both binary electron-neutral-gas-molecule collisions and collective interactions among charged particles are important. Elastic, exciting, and ionizing electron-neutral-gas-molecule collisions are included using a Monte Carlo technique. Electron-ion pairs are released in ionizing collisions. The simulation also includes the release of electron-ion pairs by photoionization. Collective interactions (space-charge effects) are included using a one-dimensional-plasma model which regards the charged particles as charge sheets. Poisson's equation is solved in one dimension based on the positions of the charge sheets to find the accelerating forces on the sheets. The method is used to simulate the growth of electron avalanches and anode- and cathode-directed streamers in nitrogen-filled parallel-plane gaps. Avalanche-simulation results are used to calculate values for the drift velocity and the ionization coefficient in nitrogen. The calculated values for these quantities agree with experimental values over a wide range of E/p , the applied electric field divided by the pressure. Velocities for anode- and cathode-directed streamers are calculated based on the streamer-simulation results. The calculated streamer velocities agree with available experimentally measured streamer velocities. The streamer-simulation results also show that photoionization is the essential mechanism for streamer formation and growth.

I. INTRODUCTION

The electrical breakdown of a neutral gas into a highly conducting ionized gas by the application of an intense electric field is an interesting physical phenomenon for many reasons. It occurs as a natural phenomenon in the case of lightning as well as in the case of high-voltage electrical-power transmission and distribution equipment where designers strive to avoid it. The phenomenon is useful in the operation of high-power high-speed switches. It is essential in the operation of electrostatic precipitators used in air-pollution control. It is one of the methods of generating and heating a plasma in controlled thermonuclear fusion machines such as the Tokamak and the Stellarator. The transient and nonlinear nature of the electrical-

breakdown phenomena, the wide range of variation of currents, particle densities, and other physical quantities of interest, and the variety of physical mechanisms responsible for the phenomena have combined to hinder the analytical quantitative understanding of such phenomena.

The simulation model, presented in this work, is based on the elementary processes of the electrical-breakdown mechanism itself and proceeds as follows: Consider two parallel plates with a voltage applied between the cathode and the anode. The space between the plates is filled with nitrogen at a given pressure. An electron, or pulse of electrons, starts near the cathode with small energy (0.5 eV) and accelerates toward the anode under the influence of the applied electric field. Elastic collisions of the electron with background-gas

molecules slow down the electron's motion toward the anode and randomize the directed kinetic energy along the electric field in all three directions. When the applied electric field is sufficiently large, the electron accelerates to high enough kinetic energies that inelastic ionizing and exciting collisions between the electron and the background gas occur. As the electron proceeds from the cathode to the anode, driven by the applied electric field, it undergoes many ionizing collisions in each of which an ion and another electron are formed. Thus, we obtain an expanding cloud of electrons traveling toward the anode, known as electron avalanche, and a cloud of ions, almost stationary in the time scale of motion of the electron avalanche, remaining behind. In order for electrical breakdown to occur, however, a secondary mechanism is necessary in order to regenerate the avalanche. From a large variety of secondary mechanisms, experimental and analytical evidence suggests that photoionization resulting from photons, released from deexcitation of excited atoms, is the most important secondary mechanism in many situations of practical interest. Photoionization enhances the electron avalanche, and luminous fronts known as streamers move toward both the anode and the cathode. In a fully formed streamer a highly conducting path is established between the anode and the cathode in a time comparable to the electron transit time, because of the role of photoionization, and electrical breakdown occurs. An alternative, but much slower, secondary mechanism for electrical breakdown is the Townsend mechanism. In this mechanism a highly conducting path is established between the anode and the cathode after a long series of successive avalanches travel through the gap. The time for breakdown in this mechanism is long compared to the electron transit time.

Early experimental studies of electrical-breakdown phenomena were carried out by Townsend and others.¹ In these early experiments continuous uv illumination was used to produce a steady electron current at the cathode in a parallel-plane gap with an applied steady electric field. The relationship between the steady-state prebreakdown electric current and the gap length in these experiments is used to determine the values of the primary- and secondary-ionization coefficients based on the Townsend mechanism of breakdown. Experimental observations of individual electron avalanches and of streamers have been carried out in electron-pulse experiments.² In these experiments a pulse of electrons is released at the cathode at the same time the voltage pulse applied to the gap reaches its plateau. The synchronization and collection of data in the electron-pulse experiments became possible with the development of high-speed switching,

oscillographic, and photographic techniques.^{2,3} Oscillographic measurement of the external circuit current of the gap is used to measure the drift velocities of electrons and ions, ionization and attachment coefficients, and electron diffusion coefficients. Experimental measurement of the spatiotemporal development of luminosity is used to measure electron drift velocities, streamer velocities, and electron diffusion coefficients.

The analytical calculation of the properties of a fully or partially ionized gas is most generally carried out by means of the distribution function $f(\vec{r}, \vec{v}, t)$ for the constituents of the ionized gas and the coupled system of Boltzmann and Maxwell equations. $f_i(\vec{r}, \vec{v}, t)$ gives the density of particles of the i th constituent in the position-velocity phase space with coordinates \vec{r} and \vec{v} as a function of time t . Frost and Phelps⁴ have investigated and developed techniques for the solution of the Boltzmann equation for electron avalanches. The technique proceeds as follows: First binary elastic, rotational, vibrational, excitational, and ionizing cross sections for electron-neutral-gas-molecule collisions are assumed as a function of electron energy. Then the electron energy distribution $f(\epsilon)$ is assumed to be spherically symmetric in velocity space to lowest order (i. e., thermal velocity \gg drift velocity). The Boltzmann equation is solved numerically for the steady state $f(\epsilon)$. The computed $f(\epsilon)$ is used to calculate the electron drift velocity, the ionization coefficient, and the diffusion coefficients. These computed transport coefficients are compared with experimentally measured values, and the results of the comparison are used to adjust the assumed collision cross sections. At high values of applied electric field divided by pressure ($E/p > 70$ in nitrogen) the electron velocity distribution is no longer spherically symmetric in velocity space; hence the Boltzmann equation can no longer be solved using the spherical harmonic-expansion technique.

Single-electron-trajectory calculations in the presence of a uniform electric field were introduced by Itoh and Musha⁵ and used to compute transport coefficients and electron-energy-distribution functions. In these calculations, single-electron trajectories are followed from the cathode to the anode while undergoing elastic and inelastic collisions with neutral-gas molecules. Collisions are decided by means of their cross sections and a Monte Carlo technique. Transport coefficients and electron energy distributions are calculated by averaging over the sequentially computed single-electron trajectories. Thomas and Thomas⁶ have improved this technique by saving the coordinates of the secondary electrons in each ionizing collision and returning to follow each of the secondary-electron trajectories. The single-electron-trajectory Monte Carlo technique is limited to the study of single avalanches

with negligible space-charge distortion.

Ward⁷ has introduced the numerical solution of one-dimensional continuity equations for electron and ion densities together with Poisson's equation for the study of electron avalanches. The electron and ion drift velocities and the ionization coefficient are assumed to be known functions of E/p , while the longitudinal diffusion term and the drift-velocity divergence term in the continuity equations are neglected. Secondary-electron emission at the cathode, due to photon and ion impact, is included in the calculations using experimentally determined secondary-ionization coefficients. This model has been applied by Ward to the study of the Townsend-breakdown mechanism for both low⁷ and high⁸ over-voltages. In the low-overvoltage case the calculated current growth and time-lag curves are in agreement with experiment. In the high-overvoltage case the calculated current growth curves vs time and luminous-front velocities are compared with experimental results of Tholl.⁹ The primary avalanche velocity is taken to be the velocity of the peak of the calculated electron-density profile. However, the experimental results of Tholl and later experimental results of Wagner^{10,11} measure the velocity of the leading edge of the luminous region which develops in their experiments. In Ref. 8, the velocity of the leading edge of the electron pulse gradually increases during the last 50 nsec of the calculation, reaching a maximum velocity approximately twice the electron drift velocity during the last 5 nsec, while the experimental leading-edge velocity increases sharply. The calculated width of the electron avalanche measured parallel to the electric field, before space-charge effects are important, is about an order of magnitude too large compared to experimental measurements.¹² There are two fundamental uncertainties in the application of this method to high-overvoltage cases where rapid spatial and temporal variations of space charge and associated electric field are important. In these cases the assumed values of the ionization coefficient and drift velocity, obtained from steady-state experiments, may not apply because of the rapid variations. The other uncertainty arises from the difference scheme used to numerically solve the continuity equations.¹³ The scheme gives results which depend sensitively on the time- and space-step sizes in the range of parameters used in Ref. 8. In particular for the primary avalanche¹⁴ (at $t = 45$ nsec before space-charge effects and secondary avalanches are important) when the spatial-step size is varied from 0.6 to 0.015 cm, the calculated electron drift velocity increases from 13.8 to 19.2 cm/ μ sec, the calculated avalanche width decreases from 0.175 to 0.07 cm, and the calculated number of electrons in the avalanche increases from 6.14×10^5 to $2.46 \times 10^6/\text{cm}^2$.

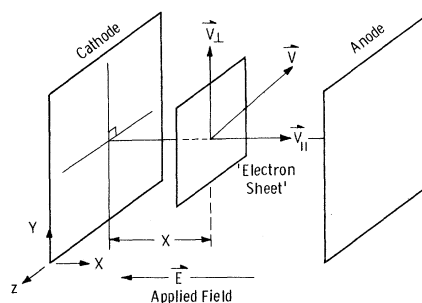


FIG. 1. Position and velocity components for a typical electron sheet. The applied electric field is also shown.

In this paper we present a new computational technique for the simulation of electrical-breakdown phenomena. The technique is applied to the simulation of single avalanches and to the simulation of anode- and cathode-directed streamers. The calculations are the first which quantitatively describe streamer formation resulting from gas photoionization. The technique also accounts for rapid spatial and temporal space-charge variations. In Sec. II the simulation model and its computational aspects are presented. Section III compares the results of single-avalanche calculations with experimental results. In Sec. IV calculated streamer formation in highly overvolted parallel-plane gaps is described and compared with experimentally measured streamer formation. Section V presents conclusions.

II. SIMULATION MODEL

The temporal development of electron and ion populations in a parallel-plane gap is calculated in the simulation by simultaneously following the trajectories of a large number of individual electrons. The simulation particles are charge sheets (see Fig. 1) that carry one or many electron charges/ cm^2 . The model is one dimensional in position space and three dimensional in velocity space. The assumption of a one-dimensional position space and a one-dimensional electric field variation simplifies the calculations and is valid for the low-pressure ($p \leq 40$ Torr) experimental conditions which are studied in this work, because high electron-diffusion rates normal to the electric field result in cylindrically symmetric linear conduction channels at these pressures. The radius of the conduction channel increases with decreasing pressure. The electron velocity distribution is assumed to be isotropic in the plane transverse to the electric field. Ions released by ionizing collisions and gas photoionization are assumed immobile because the duration of the calculations is short compared to the time scale of ion motion in the gap. This assumption is valid for single-avalanche and streamer

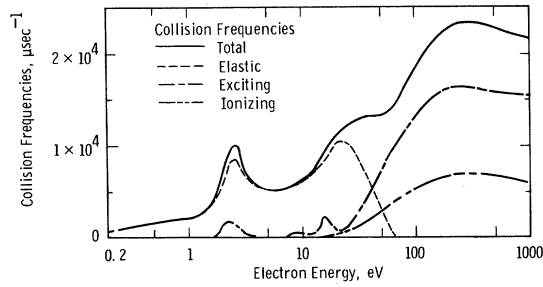


FIG. 2. Collision frequencies vs electron energy for nitrogen at pressure of 1 Torr.

calculations; however, ion motion must be included for studies of the Townsend breakdown mechanism. The gap is divided into cells to calculate the space-charge-dependent electric field. Time, the independent variable in the simulation, is advanced in equal steps Δt . At each time t_k ($t_k = k\Delta t$) a series of calculations is carried out to determine the electron positions at t_{k+1} . First, the effects of elastic and inelastic electron-molecule collisions on the electron velocities are calculated at t_k . Then the electric field is computed by solving Poisson's equation in one dimension. The electrons are accelerated by the electric field for a time Δt . Ion-electron pair release due to gas photoionization is calculated at less frequent intervals related to the rate of photoionization. In both actual and the simulation experiments the total number of electrons in the gap increases over many orders of magnitude, hence scaling is necessary to limit the number of simulation particles, each representing many electrons, that are followed.

Electron-Molecule Collision Calculations

The electron-molecule collision calculations are carried out at the beginning of each time step to compute the effect of electron-molecule collisions between t_k and t_{k+1} . The probability $P_c(t_k)$ of a collision between an electron and a neutral-gas molecule between t_k and t_{k+1} is given by

$$P_c(t_k) = 1 - e^{-\nu(t_k)\Delta t} \quad (1)$$

In Eq. (1) ν is the total collision frequency for electron-neutral-gas-molecule collisions. The total collision frequency is a function of electron energy and is the sum of the individual collision frequencies for elastic exciting and ionizing collisions:

$$\nu_{\text{total}} = \nu_{\text{elastic}} + \nu_{\text{exciting}} + \nu_{\text{ionizing}} \quad (2)$$

The collision frequencies used in the calculations are shown in Fig. 2, as functions of electron energy, for a pressure of 1 Torr. Collision frequencies for other pressures are given by the product of the collision frequency at 1 Torr and the

pressure p . The choice of the value of the time step Δt influences the total number of collisions that are generated in the computation by means of Eq. (1). In the limits of time step Δt small compared to the time between collisions [$\nu(t_k)\Delta t < 0.2$], however, the total number of collisions becomes invariant to further decreases in the time step. For example, in the case of Fig. 2, and for all electrons with energies below 100 eV, the maximum collision frequency is $\nu_{\text{max}} \sim 2 \times 10^4$ collisions/ μsec . The time step Δt , as given by $\nu_{\text{max}}\Delta t \sim 0.2$, is 10^{-5} μsec .

$P_c(t_k)$ is calculated for each electron at each time t_k and compared with a pseudorandom number, drawn from a uniform distribution on the interval (0, 1). If the random number is less than P_c , then the electron undergoes a collision; otherwise no collision occurs. When a collision occurs, it remains to decide which type of a collision it is. The ratios of particular collision frequencies to the total collision frequency are formed and ordered in the following sequence:

$$0 < \nu_{\text{elastic}}/\nu_{\text{total}} \leq (\nu_{\text{elastic}} + \nu_{\text{exciting}})/\nu_{\text{total}} \leq 1 \quad (3)$$

A pseudorandom number is generated in the interval (0, 1). The type of collision is chosen according to the interval, in the sequence of Eq. (3), into which the random number falls.

The sources for the collision frequencies used in the calculations and shown in Fig. 2 are as follows. The collision frequencies for electron energies below 20 eV are from Engelhardt, Phelps, and Risk.¹⁵ At energies above 20 eV, exciting collision cross sections are calculated by using the total energy-loss cross sections L_i of Dalgarno, McElroy, and Stewart,¹⁶ the ionizing collision cross sections of Rapp and Englander-Golden,¹⁷ and Eq. (4):

$$L_i(\epsilon) = (14 \text{ eV}) q_x(\epsilon) + (15.5 \text{ eV}) q_i(\epsilon) \quad (4)$$

In Eq. (4) $q_x(\epsilon)$ and $q_i(\epsilon)$ are the exciting and ionizing collision cross sections for electrons of energy ϵ , and the energy loss in exciting collisions is assumed to be 14 eV at all electron energies above 20 eV. The energy loss in exciting collisions by electrons with energy below 20 eV is calculated from the cross sections given in Ref. 15. The incident electron loses an energy of 15.5 eV in an ionizing collision. The remaining energy in ionizing collisions is shared between the incident and secondary (newly released) electrons. Since almost no experimental data are available concerning the sharing of energy between incident and secondary electrons in ionizing collisions equal energy sharing is assumed. Electron velocities before and after collision are related as shown in Table I. A new direction in velocity space is chosen for the incident electron (and the secondary electron in ion-

TABLE I. Electron velocities before and after collisions.

Collision type	v = velocity after collision v' = velocity before collision
Elastic	$v^2 = v'^2$
Exciting	$v^2 = v'^2 - v_x^2$
Ionizing	$v^2 = \frac{1}{2}(v'^2 - v_i^2)$

izing collisions) by randomly choosing a direction cosine ($\cos\theta$) from a uniform distribution on the interval $(-1, 1)$. Then the new velocity components are computed using Eqs. (5) and (6) along with the new total velocity already computed:

$$v_{\parallel}(t_k) = v(t_k) \cos\theta, \quad (5)$$

$$v_{\perp}(t_k) = [v^2(t_k) - v_{\parallel}^2(t_k)]^{1/2}. \quad (6)$$

The secondary electron (simulation particle) which is released in a particular ionizing collision always represents the same number of actual electrons as the incident electron (simulation particle) involved in that ionizing collision. When an ionizing collision occurs in a cell, the number of immobile positive ions in that cell is increased by an amount equal to the number of actual electrons represented by the simulation particle involved in the ionizing collision.

Electric Field and Electron Motion

The electric field in the gap is calculated at the beginning of each time step by solving Poisson's equation in one dimension. After the electron velocities have been modified by collisions as discussed above, the electrons are accelerated by the electric field for a time Δt . Collisionless-plasma simulation models¹⁸ are based on electric field and electron-motion calculations similar to those used here. Collisionless-plasma-simulation results provide a basis for choosing the spatial-cell size for the electric field calculations and a second criterion for choosing the time step in the calculations. Collisionless-plasma-simulation experience¹⁸ indicates that a time step $\Delta t = 1/4\omega_{pe}$ is small enough to give accurate results in all cases. ω_{pe} is the electron-plasma frequency given by Eq. (7):

$$\omega_{pe} = \sqrt{n} (q^2/\epsilon_0 m)^{1/2} \times 10^6 = 56 \times 10^6 \sqrt{n}, \quad (7)$$

where n is the electron density in cm^{-3} , q and m are the electron charge and mass in Coulombs and kg, and ϵ_0 is the dielectric constant of free space. The maximum time step given by $\Delta t = 1/4\omega_{pe}$ is always larger than the maximum time step given by collisional considerations for the calculations described in Secs. III and IV, hence the collisional time step is used there. Recent calculations¹⁹

indicate that for accurate results the spatial-cell size in plasma simulations must be less than the electron Debye length λ_D given by

$$\lambda_D = (\bar{v}^2/\omega_{pe}^2)^{1/2}, \quad (8)$$

where \bar{v}^2 is the mean-square electron velocity. The cell size $\Delta x = 0.02$ cm used in the calculations satisfies this requirement in all of the cases described in Secs. III and IV.

The electric field E is calculated at each time t_k , by assuming that the voltage across the gap is constant throughout each simulation experiment and that dE/dx is constant in each cell. The change in the electric field in the i th cell ΔE_i depends on the charge in that cell and is given by Eq. (9), which is equivalent to Poisson's equation:

$$\Delta E_i = \frac{1}{\epsilon_0} \sum_{\substack{\text{all sheets} \\ \text{in cell } i}} (\text{charge of each} \\ \text{electron sheet}) + Q_{+,i}; \quad (9)$$

$Q_{+,i}$ in Eq. (9) is the immobile positive charge in the i th cell due to collisional ionization and photoionization. The known gap voltage V is equal to the sum of the field in each cell times the cell width, over all N_c cells:

$$V = \sum_{i=1}^{N_c} E_i \Delta x. \quad (10)$$

The field values in adjacent cells are related by

$$E_i = E_{i-1} + \frac{1}{2}(\Delta E_{i-1} + \Delta E_i). \quad (11)$$

The field in the first cell is given by Eq. (12), where E_0 is the field at the cathode:

$$E_1 = E_0 + \frac{1}{2}\Delta E_1. \quad (12)$$

Equations (11) and (12) are substituted into Eq. (10) to relate E_0 to V and the ΔE_i 's giving

$$E_0 = V/d - \left[\sum_{i=1}^{N_c} (N_c - i + 0.5)\Delta E_i \right] / N_c. \quad (13)$$

At each time t_k , Eq. (9) is used to find the ΔE_i 's. Then E_0 is found using Eq. (13). Next, E_1 is calculated using Eq. (12). Finally, the rest of the E_i 's are calculated using Eq. (11), to complete the electric field calculations.

Once the electric field has been calculated, taking the effects of both the applied electric field and space charge into account, the motion of the electrons during the next time step is calculated using Eqs. (14) and (15), where $E = E(x(t_k))$:

$$x(t_{k+1}) = x(t_k) + v_{\parallel}(t_k) \Delta t + \frac{1}{2} (q/m) E(\Delta t)^2, \quad (14)$$

$$v(t_{k+1}) = v(t_k) + (q/m) E \Delta t. \quad (15)$$

In Eqs. (14) and (15), $t_{k+1} = t_k + \Delta t$, q/m is the electron charge to mass ratio, and x is the electron position measured from the cathode. Although the positions of electron sheets are followed in only

one dimension, as shown in Fig. 1, each electron sheet has two velocity components which are also shown in the figure. Only $v_{||}$, the parallel component of velocity, is affected by the electric field, as shown in Eq. (14). Both velocity components are altered in short-range collisions as discussed above. After new positions and velocities, at t_{k+1} , have been found for all electrons, time is advanced and the collision calculations are carried out for the next time step.

Scaling

When $N(t)$, the total number of simulation particles, exceeds the maximum allowable number of simulation particles, which is specified in the program input data, then the existing group of simulation particles is replaced by an approximately equivalent group containing fewer simulation particles. Each new particle represents several times as many actual electrons as the old particles. The old and new groups of particles should be equivalent, in the sense that their distribution in phase space is approximately equivalent.

In the simulation program a new group of "larger" particles is generated to represent the old, larger group of "smaller" particles by randomly selecting some fraction f of the old group of particles. Each of the selected particles then represents $1/f$ times as much charge and mass as each of the old particles. This technique has the advantage of simplicity and the disadvantage that there is no guarantee that the distribution of the selected particles in phase space is approximately equal to the original particle distribution. This disadvantage can be minimized by choosing the allowable number of particles and the fraction f , which is retained after a scaling, in such a way that the number of particles retained is as large as possible. The number of particles followed is limited by the available computer-memory size and partially determines the cost of the calculations.

During the early stages of the electron-pulse experiments described in Sec. IV, the number of secondary electrons due to gas photoionization is several orders of magnitude smaller than the number of electrons in the primary avalanche which develops from the electron pulse. In this case the charge sheets which are used to represent the secondary electrons carry a charge/cm² which is several orders of magnitude smaller than the charge sheets which represent the primary avalanche. As secondary avalanches develop from the secondary electrons, scaling is used to reduce the number of simulation particles which represent the secondary electrons.

Gas Photoionization

Experiments by Penney and Hummert²⁰ have mea-

sured the photoionization of a gas due to radiation emitted by an electrical discharge. The experimental results of Ref. 20 form the basis for the photoionization calculations which are described below. In the experiments a point-to-plane corona discharge is used as a radiation source. Radiation emitted by the discharge causes gas photoionization which is measured by the current to a photoelectron collector located at a distance from the corona discharge. The experimental results show that the photoionization rate in the collection region is proportional to the rate of ionizing electron-neutral-gas-molecule collisions in the discharge. Since the collision calculations described above provide an estimate of the collisional-ionization rate at all points in the gap, in the computer simulation, the experimental data described above can be used to estimate the rate of photoion-pair production in the gap.

The photoionization calculations are based on Eq. (16) which relates N_{p_i} , the number of photoion pairs (photoelectrons and photoions) produced in the i th cell during a time period Δt_p , to N_{D_j} , the number of ionizing collisions in the j th cell during the same time period:

$$N_{p_i} = \sum_{j=1}^{NC} \psi_{ij} p \Delta x \theta_{ij} N_{D_j}. \quad (16)$$

In Eq. (16) p is the pressure, Δx is the cell length, θ_{ij} is the solid angle subtended at cell j by cell i , and ψ_{ij} is an experimentally measured coefficient from Ref. 20. The photoionization calculations are carried out at successive times t_{p_r} ($t_{p_r} = r \Delta t_p$). Δt_p , the time step for the photoionization calculations, is chosen larger than Δt , the time step for collision calculations, so that $N_{p_i} \geq 1$ in Eq. (16). The radius R_{GAP} of the region where photoion release is calculated, is fixed in the simulations at 0.5 cm. A fixed radius allows θ_{ij} in Eq. (16) to be calculated and is equivalent to ignoring photoion pairs that are produced outside a cylindrical region with radius R_{GAP} .

The simulation model described in this section can be used for physical situations where both space-charge effects and collisional effects are important in contrast to the spherical-harmonic-expansion technique of Refs. 4 and 15 and the Monte Carlo technique of Ref. 6, which are limited to the study of space-charge-free situations, and in contrast to the plasma-simulation models of Ref. 18, which are limited to the study of collisionless plasmas. The simulation model described here is useful for the calculation of both steady-state and time-varying electron energy distributions because all of the electrons trajectories are followed simultaneously in time. Since the model incorporates realistic particle densities, collision

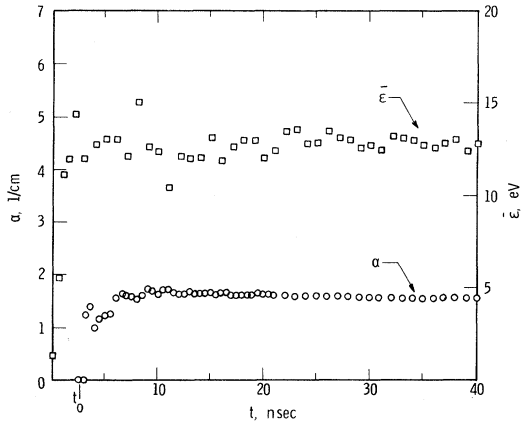


FIG. 3. Mean energy $\bar{\epsilon}$ and ionization coefficient α vs time for a simulation experiment where the ratio of the applied electric field to pressure $E/p=300$ V/cm Torr, the pressure $p=0.5$ Torr, and the initial number of electrons $N(t=0)=50$.

cross sections, and correctly accounts for space-charge effects, the results calculated using this model are expected to be in good agreement with experimental results, if all the fundamental mechanisms are taken into account.

III. ELECTRON-AVALANCHE RESULTS

In both simulated and actual electron-pulse experiments leading to single avalanches, the number of electrons N in the avalanche increases exponentially with time as a result of ionizing collisions:

$$N(t) = N(t_0) e^{\alpha v_d (t-t_0)}, \quad (17)$$

where α is the first Townsend ionization coefficient, and v_d is the electron drift velocity given, for $t > t_0$, by

$$\alpha = \ln[N(t)/N(t_0)] / [\bar{x}(t) - \bar{x}(t_0)], \quad (18)$$

$$v_d = [\bar{x}(t) - \bar{x}(t_0)] / (t - t_0), \quad (19)$$

where $\bar{x}(t)$ is the average electron position, and t_0 is the time required for the avalanche to reach a steady state as shown in Fig. 3. This figure shows the variation of α and the average electron energy $\bar{\epsilon}$ with time. t_0 is the time required for the average electron energy to reach its steady-state value. There is a time lag between the onset of steady state for the average energy and the onset of steady state for the ionization coefficient. The transient in α occurs because initially, $t \sim t_0$, the number of accumulated ionizing collisions is small, hence the ionization coefficient has not reached steady state. Figure 3 also shows that the mean electron energy fluctuates, with diminishing amplitude of fluctua-

tion, because the number of electrons in the avalanche is small in order to reduce computational costs. The drift velocity, calculated using Eq. (19), has the same qualitative time behavior as α , but reaches steady state in a shorter time.

When space-charge distortion does not occur, both actual experiments and simulation experiments show that α/p and v_d depend on E/p , the ratio of the applied electric field to the pressure. When E_p in V/cm Torr and the gap length d in cm are adjusted in the simulation experiments, so that $\alpha d = \alpha v_d t_d \lesssim 4$, space-charge distortion does not occur. The multiplication factor ($e^{\alpha d}$) at $t = t_d$, when the avalanche reaches the anode, is less than 55, and the computer-memory economy allows one electron charge/cm² per simulation particle. Typically the electron pulse released at the cathode contains 5 to 50 simulation particles.

Figures 4 and 5 show the variation of the drift velocity v_d and the ionization coefficient α divided by the pressure p , as functions of E/p . The solid lines are published experimental data,²¹⁻²⁴ and the points are the simulation results. The very good agreement between experimental data and the simulation results shown in Figs. 4 and 5 indicates that the collision calculations accurately predict the growth of electron pulses into electron avalanches. The data generated by the simulation technique also give the longitudinal diffusion coefficient for electrons and the electron-energy-distribution function in very good agreement with experiment as shown in Ref. 25. A current-voltage characteristic for a given gap spacing d and pressure p can also be obtained by plotting the

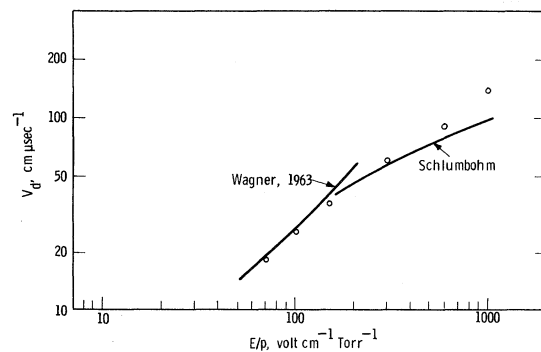


FIG. 4. Calculated and experimental values of v_d , the electron drift velocity, vs E/p . Experimental results are shown as smooth curves. Calculated results are shown as points. The pressures for the calculations in Torr are 0.2 for $E/p=1000$ and 600, 0.5 for $E/p=300$, and 1 for $E/p=150$, 100, and 70. The simulation particles carry one electron charge/cm² in all cases. The number of particles released at the cathode is 5 for $E/p=1000$; 50 for $E/p=600$, 300, and 150; 200 for $E/p=100$; and 250 for $E/p=70$. Experimental curves are identified by author.

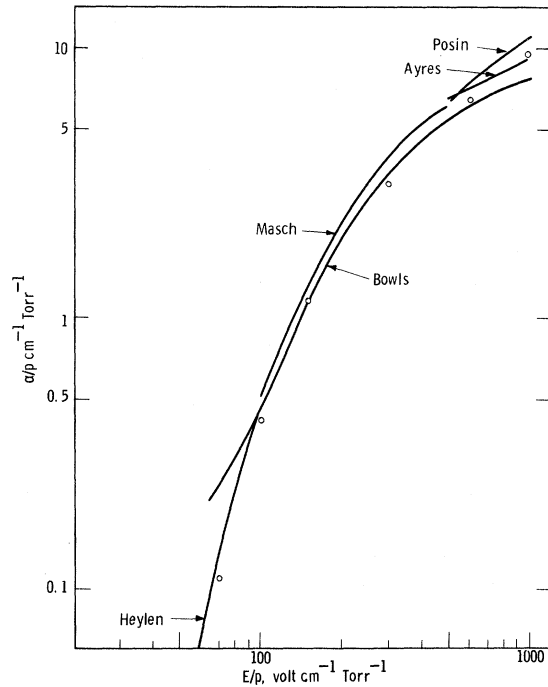


FIG. 5. Calculated and experimental values of α/p , the first Townsend ionization coefficient divided by pressure vs E/p . Experimental results are shown as smooth curves. Calculated results are shown as points. The pressures and initial number of simulation particles are the same as those in Fig. 4. Experimental curves are identified by author.

maximum electron current versus the applied gap voltage assuming that the time constant of the external circuit is small compared to $1/\alpha v_d$. A current-voltage characteristic is shown in Fig. 2 of Ref. 26.

When E/p is held fixed but p is increased, α increases. At higher pressures $\alpha d \gtrsim 4$, and simulation particles with many electron charges/cm² must be used. The calculated values of α/p and v_d are approximately equal for cases with $\alpha d \gtrsim 4$ (compared to cases with $\alpha d < 4$) as long as space-charge distortion of the applied electric field does not occur. Experimental² and simulation results indicate that for $\alpha d \gtrsim 14$, space-charge distortion becomes important. In this case, both α and v_d lose their usefulness because the number of electrons no longer grows exponentially with time, and v_d is no longer constant in time or space. The detailed effects of space charge can be observed and measured in the simulation whereas experimental measurement is difficult.

The simulation technique and the data it generates describe the full range of dynamic phenomena for electron avalanches. This technique can be used to establish the maximum value of E/p for which the Lorentz approximation is valid. This

technique, compared to the techniques of Refs. 5 and 6, not only takes into account space-charge effects but also is easier to use for studying the transient phase of avalanche formation.

IV. ANODE- AND CATHODE-DIRECTED STREAMER RESULTS

Gas photoionization was first proposed by Raether² and by Meek²⁷ as the secondary mechanism leading from a single avalanche to streamer formation and electrical breakdown. Quantitative experimental measurements of streamer formation in short (~ 3 cm) parallel-plane gaps have been carried out by Tholl⁹ and Wagner.^{10,11} Wagner¹¹ also gives a qualitative description of streamer formation, but no quantitative theoretical calculations, relating streamer formation and evolution to elementary mechanisms, exist in the literature. The qualitative description of streamer formation given by Wagner¹¹ is shown schematically in Fig. 6. This figure shows that streamer development does not begin until the primary avalanche reaches a critical size ($N \approx 10^9$ electrons). The position $\bar{x}_{\text{critical}}$ where the critical size is reached is given (as found from experiment^{10,11}) by $\ln N(t=0) + \alpha \bar{x}_{\text{critical}} \approx 20$. The experimental results of Penney and Hummert²⁰ demonstrate that the rate of photoionization in a gas is proportional to the rate of collisional ionization, which is in turn proportional to the number of electrons present. The coefficient of proportionality, $\psi p \Delta x \theta$ in Eq. (16), is always less than 10^{-3} ; hence a primary avalanche must contain a minimum number of electrons for the release of the number of secondary electrons required for streamer formation.

Figure 7 shows the calculated growth of the number (per cm²) of electrons in the primary avalanche

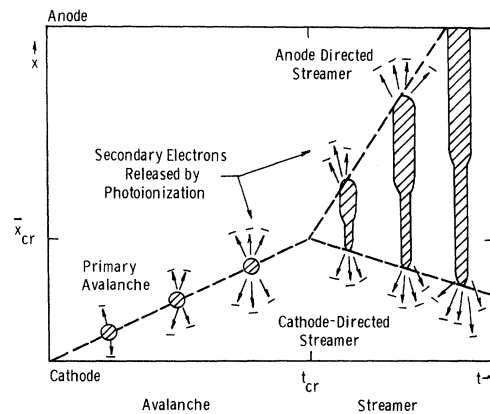


FIG. 6. Schematic representation of the qualitative description of streamer development given by Wagner. (Based on Figs. 22 and 27 of Ref. 11.) Anode- and cathode-directed streamer propagation begins at t_{critical} when the avalanche position equals $\bar{x}_{\text{critical}}$.

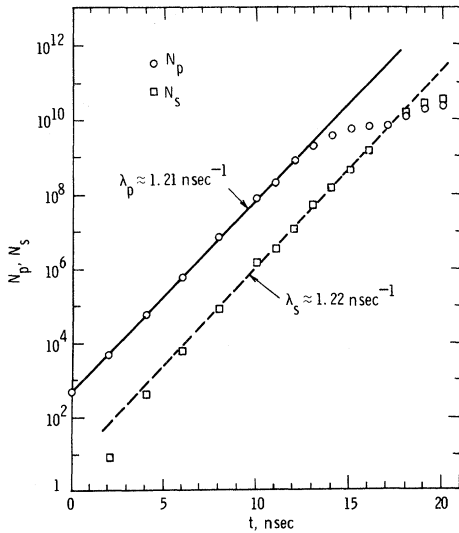


FIG. 7. Calculated number of primary electrons, N_p , and number of secondary electrons, N_s , vs time t for a simulation experiment where the ratio of applied field to pressure $E/p=1000$ V/cm Torr, the pressure $p=1$ Torr, the initial number of electrons $N(t=0)=500$, and the gap length $d=4$ cm. Space-charge distortion of the applied electric field begins in this case at $t \approx 7$ nsec when $\ln N(t=0) + \alpha \bar{x} = 14.7$ and the total number of electrons $N = 2.1 \times 10^6$. The growth rates $\lambda_p \approx \lambda_s \approx 1/\alpha v_d = 1.23$ nsec $^{-1}$. The time-step and spatial-cell size used are $\Delta t = 2.5 \times 10^{-5}$ μ sec and $\Delta x = 0.02$ cm. The photoionization and luminosity time steps are, respectively, $\Delta t_p = 1 \times 10^{-3}$ μ sec and $\Delta t_x = 5 \times 10^{-4}$ μ sec.

and the calculated growth of the number of secondary electrons in secondary avalanches for a particular simulation experiment. All of the electrons in the primary avalanche grow from the initial electron pulse by collisional ionization. The secondary avalanches are initiated by photoelectrons and grow by means of collisional ionization. Figure 7 shows that the number of primary electrons N_p grows exponentially with time for $0 < t \lesssim 12.5$ nsec, and that N_s , the number of secondary electrons, grows exponentially with time for $4 \text{ nsec} \lesssim t \lesssim 17.5$ nsec. The growth rates for primary and secondary electrons are both approximately equal to $1/\alpha v_d$ [see Eq. (17)]. The growth rate for N_p is reduced, for $t \gtrsim 12.5$ nsec, by a space-charge field which reduces the net electric field in the region of the primary avalanche. Most of the secondary electrons are in regions where the net electric field is greater than or equal to the applied field for $t \lesssim 17.5$ nsec; hence N_s continues to grow at a high rate. At $t \approx 17.5$ nsec the region of reduced electric field reaches the anode, and the growth rate of N_s is reduced as the number of secondary electrons in regions of low net electric field increases.

Figure 8 shows the electric field at three successive times for the case of the simulation experi-

ment of Fig. 7. This figure shows that a region of reduced electric field develops and grows in the simulation experiment. The region of reduced electric field corresponds to the region of high electron and ion densities, where a plasma has been formed, and the electrons have reduced mean energy and drift velocity. The electric field at the anode is at first enhanced and then decreased abruptly when the plasma reaches the anode. The electric field at the cathode increases monotonically as the developing plasma moves toward the cathode also. The electric field shown in Fig. 8 was calculated assuming a constant applied voltage across the gap and is based on a one-dimensional calculation as discussed in Sec. II. The anode field is $\sim 10\%$ higher than the cathode field at $t = 12$ nsec because the unoptimized scaling procedure used in this calculation does not conserve particles exactly, resulting, in this case, in an excess of electrons of $\sim 5\%$ at $t = 12$ nsec. The effect of the scaling procedure on the electric field is negligible compared to the effect of the developing plasma region and the loss of electrons at the anode. In this calculation the effect of the external-circuit impedance on current flow and the resulting modification of the gap voltage were not taken into account. These effects can easily be included in the calculation when the external-circuit parameters are known.

The light emitted by developing avalanches and streamers is due to the photons emitted by excited molecules, when they return to a lower state. In the computer simulation experiments the number of excited molecules in each cell is increased each time an excited collision occurs in that cell. The density of excited molecules is printed out and reset to zero at times t_{x_s} ($t_{x_s} = s \Delta t_x$). The excited-molecule number density that is printed out at each time t_{x_s} gives the number density of excited molecules which have been produced between $t_{x_{s-1}}$ and t_{x_s} . This procedure corresponds to the relaxation of excited molecules in the experiments,

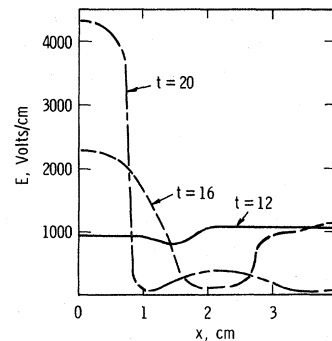


FIG. 8. Calculated electric field vs position at $t=12$, 16, and 20 nsec for the same conditions as Fig. 7.

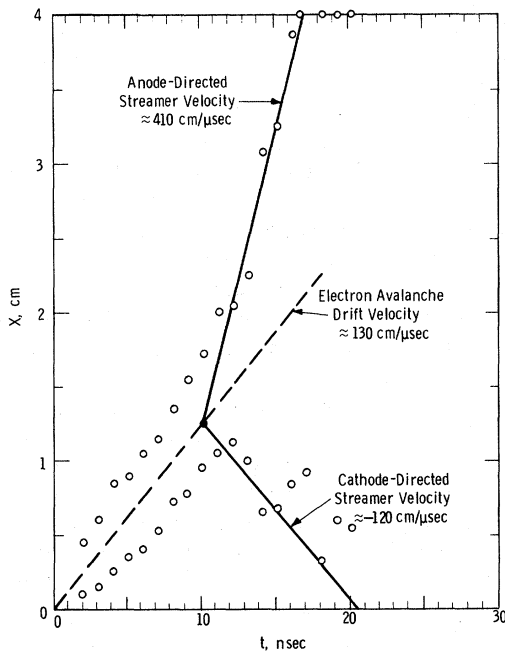


FIG. 9. Calculated luminosity vs position and time for the same conditions as in Fig. 7. The points are the leading and trailing edges (where the luminosity falls to two orders of magnitude below the peak luminosity) of the luminous region at each time. Streamer development begins at $t \approx 12.5$ nsec when $\ln N(t=0) + \alpha \bar{x} = 21.3$ and the total number of electrons $N = 1.42 \times 10^9$.

with the excited molecules returning to the ground state with an average lifetime approximately equal to Δt_x . The spatial density of excited molecules at successive times is taken as an estimate of the spatial density of the light emitted by the simulated avalanche or streamer at the same times.

Wagner^{3,10,11,28} has measured the luminosity of developing avalanches and streamers, and the propagation velocities of anode- and cathode-directed streamers. The streamer velocities are the propagation velocities of the luminous fronts observed by Wagner and shown schematically in Fig. 6. The boundaries of the luminous region for simulated streamers are assumed, at each time, to be the points where the excited-molecule density falls to two orders of magnitude below its peak value. Figure 9 shows that both boundaries of the luminous region propagate toward the anode for $t < t_{critical} \approx 12.5$ nsec. At $t \approx 12.5$ nsec the propagation velocity of the anode-side boundary abruptly increases, and the cathode-side boundary reverses direction and moves toward the cathode. The calculated value of the quantity $[\ln N(t=0) + \alpha \bar{x}] = 21.3$, in the simulation, at $t = 12.5$ nsec, in agreement with experimental results^{10,11} which show that streamer propagation begins when $[\ln N(t=0) + \alpha \bar{x}_{critical}] \approx 20$. When the anode- and cathode-directed streamer

velocities are normalized in a coordinate system moving with the electron drift velocity, as suggested by Wagner,^{10,11} they are approximately equal. The normalized anode- and cathode-directed streamer velocities are given by Eqs. (20) and (21), respectively:

$$\Delta v_a = (v_a - v_d) / v_d, \quad (20)$$

$$\Delta v_c = (v_c - v_d) / v_d. \quad (21)$$

Experimental^{10,11} results show that $\Delta v_a \approx |\Delta v_c|$. For the data of Fig. 9, $\Delta v_a = 2.1$ and $|\Delta v_c| = 1.9$.

Figure 10 shows the luminosity which develops in a simulation experiment, which is identical to the simulation experiments of Figs. 7-9, except that photoionization was omitted from the calculations. Comparison of Figs. 9 and 10 shows that photoionization is the essential mechanism in streamer development.

Calculated and experimental¹¹ anode-directed streamer velocities are shown vs E/p in Fig. 11 for several pressures. Table II summarizes the corresponding calculated anode- and cathode-directed streamer velocities and normalized streamer velocities. Calculated and experimental²¹ values of the primary-avalanche electron drift velocity are also shown in Fig. 11 for $50 \leq E/p \leq 1000$. Figure 11 shows that the calculated anode-directed streamer velocity varies exponentially with E/p at all pressures, in agreement with ex-

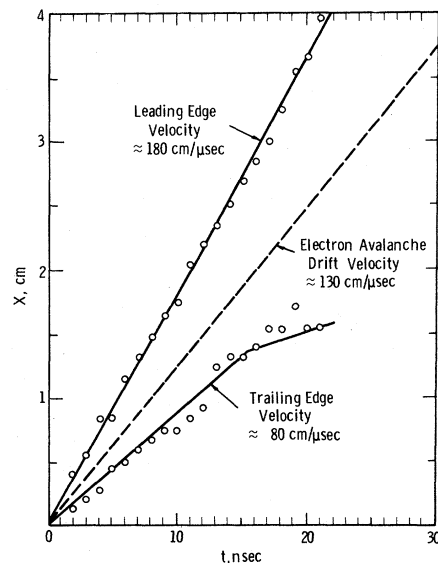


FIG. 10. Calculated luminosity vs position and time for the same conditions as in Figs. 7-9 except that photoionization was omitted from the calculations. The points are the leading and trailing edges at the luminous region (determined as described in Fig. 9) at each time. Space-charge distortion of the applied electric field begins at $t \approx 7$ nsec.

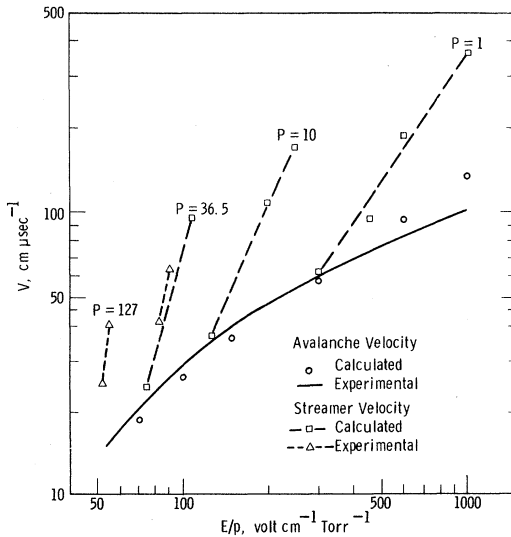


FIG. 11. Calculated and experimental avalanche and streamer velocities. The initial number of electrons $N(t=0) = 500$ in all cases. The gap length was $d = 4$ cm for $p = 1$ Torr, and $d = 3$ cm for $p = 10$ and 36.5 Torr. The calculated avalanche velocities are for $p = 1$ Torr.

periment.^{10,11} The experimental data of Refs. 11 and 21, shown in Fig. 11, do not show the transition from avalanche drift velocity to anode-directed streamer velocity. However, later experimental data of Wagner²⁸ show a smooth transition from an avalanche to an anode-directed streamer in agreement with the calculated results shown in Fig. 11. The calculated values of Δv_a and $|\Delta v_c|$ shown in Table II are approximately equal for all cases ($\Delta v_a / |\Delta v_c| \approx 1$) in agreement with experimental results^{10,11} which also show that $\Delta v_a \approx |\Delta v_c|$.

The streamer-simulation results strongly suggest that photoionization is the essential mechanism in streamer development. Streamers do not develop when photoionization is omitted from the calculations. On the basis of the data presented in Figs.

7–9 and Fig. 6 of Ref. 29, which shows exciting collision densities at successive times, the following mechanism for streamer formation becomes evident. Initially the primary avalanche grows and drifts to the mid-gap region. At the same time secondary avalanches, owing to photoionization, grow ahead of and behind the primary avalanche. When the primary avalanche reaches a size of approximately 10^9 electrons, space-charge effects slow its growth. Secondary avalanches continue to grow, both ahead of and behind the primary avalanches, with the result that the region of high electron and ion density and high luminosity (plasma region) propagate toward the anode and toward the cathode. When the plasma region reaches the anode, the secondary-avalanche growth is also slowed. The plasma region also moves toward the cathode resulting in a high electric field region between it and the cathode.

V. CONCLUSIONS

The computer simulations described are the first plasma simulations which include realistic binary electron-neutral-gas-molecule collision effects, photoionization, and collective interactions among charged particles. Binary electron-neutral-gas-molecule collisions are the essential mechanism in electron-avalanche growth. The simulation results give values for electron drift velocity, ionization coefficient, longitudinal diffusion coefficient, and electron energy distribution as functions of time and space for avalanches. The good agreement between calculated and measured electron-avalanche drift velocities and ionization coefficients demonstrates the validity of the binary collision-simulation techniques.

The good agreement between calculated and measured streamer velocities strongly suggests that photoionization is the essential mechanism in streamer formation and demonstrates the validity of the photoionization-simulation technique. The

TABLE II. Streamer-simulation results.

E/p (V/cm Torr)	p (Torr)	v_a (cm/ μ sec)	v_c (cm/ μ sec)	Δv_a	v_c (cm/ μ sec)	Δv_c	$\Delta v_a / \Delta v_c $
1000		130	400	2.1	-120	-1.9	0.91
600	1	90	180	1.0	0	1.0	1.0
450		77	96	0.25	55	0.29	0.86
300		56	60	0.072	52	0.072	1.0
250		45	170	2.8	-50	-2.1	1.3
200	10	43	100	1.3	0	1.0	1.3
125		30	36	0.20	23	0.23	0.87
110	36.5	25	95	2.8	-48	-2.9	0.97
75		18	23	0.28	13	0.28	1.0

simulation technique developed in this paper can be extended to study other electrical-breakdown and plasma-formation phenomena, such as electrical breakdown in nonuniform field gaps, glow to arc transitions, laser breakdown in gases, laser-plasma heating, and ohmic heating in Tokamak and Stellarator machines for controlled thermonuclear fusion.

ACKNOWLEDGMENTS

The authors acknowledge with pleasure and thank Professor G. W. Penney and Dr. A. V. Phelps for many helpful discussions. This paper is based partially on a thesis submitted by one of the authors (L. E. K.) to Carnegie-Mellon University, Pittsburgh, Pa., in partial fulfillment of the requirements of the Ph. D. degree.

*Work supported by the Air Force Office of Scientific Research under Grant No. AFOSR-69-1708.

†Present address: Westinghouse Research Laboratories, Pittsburgh, Pa. 15235.

¹J. S. Townsend, *Electrons in Gases* (Hutchinson's, London, 1947), Chap. 5.

²H. Raether, *Electron Avalanches and Breakdown in Gases* (Butterworths, London, 1964).

³K. H. Wagner, in *Proceedings of the Sixth International Conference on Phenomena in Ionized Gases, Paris, 1963* (European Atomic Energy Community, Paris, 1964), Vol. 2, p. 309.

⁴L. S. Frost and A. V. Phelps, *Phys. Rev.* **127**, 1621 (1962).

⁵T. Itoh and T. Musha, *J. Phys. Soc. Japan* **15**, 1675 (1960).

⁶R. W. L. Thomas and W. R. L. Thomas, *J. Phys. B* **2**, 562 (1969).

⁷A. L. Ward, *Phys. Rev.* **138**, A1357 (1965).

⁸A. L. Ward, *J. Appl. Phys.* **36**, 2540 (1965).

⁹H. Tholl, *Z. Naturforsch.* **18a**, 587 (1963).

¹⁰K. H. Wagner, in *Proceedings of the Seventh International Conference on Phenomena in Ionized Gases, Belgrade, 1965* (Gradevinska Knjiga, Beograd, 1966), Vol. 1, p. 571.

¹¹K. H. Wagner, *Z. Physik* **189**, 465 (1966).

¹²The width r of the avalanche at time $t=45$ nsec, before space-charge distortion of the applied electric field occurs, is given by $r=(2D_L t)^{1/2}=0.012$ cm; $D_L=(D_L/\mu)(v_d/E)=1550$ cm²/sec. The values of $\mu=v_d/E=816$ cm²/V sec and $E/p=49$ V/cm Torr are taken from Ward (Ref. 8). The value of $D_L/\mu=1.9$ V at $E/p=49$ V/cm Torr is given by Lowke and Parker [J. J. Lowke and J. H. Parker, Jr., *Phys. Rev.* **181**, 302 (1969)].

¹³K. V. Roberts and N. O. Weiss, *Math, Comp.* **20**, 272 (1966).

¹⁴L. E. Kline, Westinghouse Research Report (to be

published).

¹⁵A. G. Engelhardt, A. V. Phelps, and C. G. Risk, *Phys. Rev.* **135**, A1566 (1964).

¹⁶A. Dalgarno, M. B. McElroy, and A. I. Stewart, *J. Atmospheric Sci.* **26**, 753 (1969).

¹⁷D. Rapp and P. Englander-Golden, *J. Chem. Phys.* **43**, 1464 (1965).

¹⁸This value for Δt is given by R. Morse, in *Methods in Computational Physics* (Academic, New York, 1970), Vol. 9, p. 231.

¹⁹D. Montgomery and C. W. Neilson, *Phys. Fluids* **13**, 1405 (1970).

²⁰G. W. Penney and G. T. Hummert, *J. Appl. Phys.* **41**, 572 (1970).

²¹H. Schlumbohm, *Z. Physik* **182**, 317 (1965).

²²The ionization coefficient values of Masch, Ayres, and Posin are tabulated in D. Q. Posin, *Phys. Rev.* **50**, 650 (1936).

²³W. E. Bowls, *Phys. Rev.* **53**, 293 (1938).

²⁴A. E. D. Heylen, *Nature* **183**, 1545 (1959).

²⁵L. E. Kline and J. G. Siambis, in *Proceedings of the Tenth International Conference on Phenomena in Ionized Gases, Cambridge, 1971* (Donald Parson, Oxford, 1971), p. 53.

²⁶L. E. Kline and J. G. Siambis, *Proc. IEEE* **59**, 707 (1971).

²⁷J. M. Meek, *Proc. Inst. Elec. Engrs. (London)* **116**, 1 (1969).

²⁸K. H. Wagner, in *Proceedings of the Ninth International Conference on Phenomena in Ionized Gases, Bucharest, 1969* (Editura Academiei Republic Society, Bucharest, 1969), p. 265.

²⁹J. G. Siambis and L. E. Kline, in *Proceedings of the Tokyo 1971 AICA Symposium on Simulation of Complex Systems* (Association Internationale Calcul Analogique, Paris, 1971), paper F-10.